2020 25th International Conference on Pattern Recognition (ICPR)
Milan, Italy, Jan 10-15, 2021

A new geodesic-based feature for characterization of 3D shapes: application to soft tissue organ temporal deformations

Karim Makki[1,⋆] , Amine Bohi[1], Augustin .C Ogier[1], Marc Emmanuel Bellemare[1]
[1] Aix Marseille Univ, Université de Toulon, CNRS, LIS, Marseille, France

***Abstract*—Spatio-temporal feature descriptors are of great importance for characterizing the local changes of 3D deformable shapes. In this study, we propose a method for characterizing 3D shapes from point clouds and we show a direct application on a study of organ temporal deformations. As an example, we characterize the behavior of the bladder during forced respiratory motion with a reduced number of 3D surface points: first, a set of geodesically equidistant points representing the vertices of quadrilateral mesh for the organ surface are tracked throughout a long dynamic MRI sequence using a large deformation diffeomorphic metric mapping (LDDMM) framework. Second, a novel 3D shape descriptor invariant to translation, scale and rotation is proposed for characterizing the temporal organ deformations by employing an Eulerian Partial Differential Equations (PDEs) methodology. We demonstrate the robustness of our feature on both synthetic 3D shapes and realistic dynamic Magnetic Resonance Imaging (MRI) data sequences portraying the bladder deformation during a forced breathing exercise. Promising results are obtained, showing that the proposed feature may be useful for several computer vision applications such as medical imaging, aerodynamics and robotics.**

***Index Terms*—LDDMM, PDEs, eigen analysis, motion estimation, high-resolution reconstruction**

I. Introduction

Computer vision, pattern recognition, and image processing techniques have played a crucial role in the development of several healthcare applications such as clinical data acquisition and post-processing. In this paper, we propose a generic pipeline for the characterization of highly deformable 3D shapes. As an application, we characterize the bladder dynamics during forced respiratory motion to help surgeons and clinicians for better understanding the pelvic floor disorders, frequently occuring in women older than 50 years. This clinical context is the primary motivation of this work, the results of which go beyond this framework and can be generalized to any 3D shapes.

Dynamic MRI is a non-invasive imaging technique that has made it possible to explore the pelvic floor system during respiratory motion. However, dynamic MRI suffers from its low-resolution (LR) in addition to its sensitivity to motion artifacts. In the literature, only a few studies have attempted to track pelvic organ deformations *in vivo*. Rahim et al. [1] proposed a diffeomorphic mapping based characterization of temporal dynamic MRI sequences to quantify the temporal deformation of the pelvic floor organs in 2D+t. However, a more informative 3D+t quantification of their dynamics is necessary because of the large shape variability of the pelvic organs across time. To overcome these limitations, a combination of spatial resolution of conventional static MRI and temporal resolution of dynamic MRI data is necessary. First studies for estimating dense deformation fields from a static MRI scan to a set of LR dynamic MRI scans are presented in [2], [3] in the context of articulated polyrigid registration of human joints. A similar study to perform a high-resolution (HR) temporal reconstruction of the bladder volume during loading exercises is recently proposed in [4]. Promising results have been obtained, showing the bladder in its 3D complexity during deformation due to strain conditions with an estimation of the most deformed tissue areas. In this work, we propose to exploit the full potential of such reconstructed data for characterizing the bladder deformations in the HR domain. For a compact shape representation, we parameterize the reconstructed organ surface with a reduced number of points representing the vertices of a temporal quadrilateral mesh in order to use the generated (3D+time) smooth mesh sequence for finite element simulations. This configuration is then required for establishing a robust biomechanical model of organ dynamics [5]. Since the mesh vertices can be considered as a 3D point cloud, we analyse a set of common covariance-based features incorporating the concept of "neighborhood of a point", introduced in [6] and applied in [7]–[9], pinpointing some limitations regarding their sensitivity to noise and their dependency on point cloud density. Instead, we propose a different feature type based on the optimal geodesic path that maps the moving surface point to its corresponding one in the surrounding sphere in order to evaluate the local shape variability around that point. In [10], *Yezzi et al.* introduced a robust Eulerian PDE approach for computing the thickness of soft tissues based on the solution of Laplace's equation between two non-intersecting boundaries. In this work, we extend this approach to compute geodesic distances and shortest paths and curves from an arbitrary shape to its surrounding sphere in order to derive a new geometric feature which is invariant to *translation*, *scaling*, and *rotation*. Obtained results on synthetic shapes demonstrate that the proposed feature outperforms traditional covariance-based features.

⋆This research was supported in part by the AMIDEX - Institut Carnot STAR under the DynPelvis3D grant.

978-1-7281-8808-9/20/$31.00 ©2020 IEEE

2020 25th International Conference on Pattern Recognition (ICPR) | 978-1-7281-8808-9/21/$31.00 ©2021 IEEE | DOI: 10.1109/ICPR48806.2021.9412922

II. Related work

A. Point cloud tracking

Point cloud tracking has led to many significant advances in many computer vision applications such as robotics [11], astronomy [12] and medical imaging [1]. Tracking a set of points can be formulated as a registration problem where the goal is to align between two point sets representing a 3D shape at two different times. The Iterative Closest Point algorithm, originally proposed in [13] for estimating a global linear transformation to align two point sets, has been extended for non-linear registration of large 3D point sets based on a statistical expectation–maximisation (EM) algorithm [14]. However, robustifying this algorithm face to local minima problems occuring during the optimization of cost function remains a challenging task. The LDDMM registration framework [15] has made it possible to estimate smooth continuous-time trajectories mapping between two point clouds without having to use point-to-point correspondence. This parametric Riemannian-based framework can deal with large deformations, yielding geometric transformations characterized with a list of nice algebraic properties such as *smoothness*, *differentiability*, and *invertibility*. The LDDMM introduced in [16] has been extended to several applications: a Bayesian atlas application is proposed in [17]. A geodesic shape regression with multiple geometries and sparse parameters is presented in [18]. In [15], the authors have detailed a scheme for parallel transport on a high-dimensional manifold of diffeomorphisms based on the LDDMM. In this work, we propose to employ the LDDMM to estimate a smooth continuous curves of highly-deformable shapes represented with a set of sparse parameters (*i.e.* the surface S is sampled using a set of points $\{x_i\}_{i=1}^{N}$).

B. Feature extraction from 3D point cloud data

Feature extraction is a crucial process in every knowledge representation and classification [19]. In particular, most studies working on point clouds are based on an eigenanalysis method employing features derived from a local structure tensor, *i.e. local covariance matrix* calculated from each point neighborhood. These matrices represent a second-order invariant moments within the point positions [6], [8], [20]. The local covariance matrix is defined on a k-neighborhoods of a given point p according to:

$$C(p) = \frac{1}{k}\sum_{i=1}^{k}(p_i - \overline{p})(p_i - \overline{p})^T \tag{1}$$

where $\{p_i\}_{i\in\{1\ldots k\}}$ are the k nearest neighbor points to the point p, and $\overline{p}$ holds the centroid of the neighbors $\{p_i\}_{i\in\{1\ldots k\}}$.

The obtained covariance matrix at each point is symmetric and positive semi-definite. The eigenvectors $\{e_1, e_2, e_3\}$ of the covariance matrix together with their corresponding eigenvalues $\{\lambda_1, \lambda_2, \lambda_3\}$ allow to locally estimate the surface variation. Assuming that the eigenvalues of $C(p)$ are sorted as follows: $0 \leq \lambda_1 \leq \lambda_2 \leq \lambda_3$, some of the covariance-based features are: the anisotropy: $A_\lambda = \frac{\lambda_3 - \lambda_1}{\lambda_3}$; and the curvature: $C_\lambda = \frac{\lambda_1}{\lambda_1+\lambda_2+\lambda_3}$.

These geometric features have been used in many applications such as point-sampled surfaces simplification [6], 3D point cloud classification [21], and recently used for detection and characterization of defects on airplane exterior surfaces [8]. The key idea of this approach is to derive geometric features from a suitably chosen neighborhood size. However, the optimal neighborhood size is hardly predictable [22] and the proposed features may not be robust and effective enough for some complex geometries.

The geodesic distance is of great importance for solving many computer vision problems such as surface segmentation into regions called Voronoi cells, sampling of surface points at regular geodesic distance, and meshing a 3D surface with geodesic Delaunay triangles. In the work of Peyré et al. [23], the optimal geodesic curve mapping between two surface points is obtained using Riemannian metric tensors by integrating an ordinary differential equation (ODE) modeling the spatio-temporal evolution of surface variation using the Riemannian Eikonal equation. To cope with the dependency of numerical accuracy on the size of vertex neighborhood used for deriving local tensors, we propose in this work a level set method for mapping a shape to a sphere by minimizing a Dirichlet energy. Equivalent for curves of heat equation and independent of parameterization, it can be used for evaluation of surface variation using an Eulerian PDE approach (extrinsic), with no need to evaluate the Riemannian tensor (intrinsic curvature) which not only incurs high computational costs [24], but also impacts numerical stability during motion.

III. Methods

A. Dynamic quadrilateral mesh

1) Quadrilateral mesh generation: In this part, we first extracted iso-surfaces from the reconstructed organ volumes (*i.e.* 3D binary masks) at the first time frame using the marching cubes algorithm. The marching squares/cubes is the standard algorithm to extract iso-curves/surfaces from a discretized image/volume [25]. Then, and to take into account the complexity of the organ shape, a topologically regular quadrilateral mesh of the organ surface is generated for the first reconstructed volume in the sequence, using a robust algorithm presented in [26]. This algorithm is robust enough to establish a convex quad mesh for the organ surface since it avoids irregularity problems at the poles, as encountered in [27], despite some singularities which can be regularized by mesh upsampling in order to obtain a pure quad mesh. Fig. 1 illustrates the quality of the obtained mesh. Then, we propose to track the mesh vertices while preserving their connections (*i.e.* while keeping the faces unchanged). This allows for constructing a spatio-temporal structured meshes which might be used later for deriving some biomechanical properties of the organ dynamics such as distortion, elongation and stresses using finite element methods which are required for establishing a biomechanical model for the organ dynamics.

2) Estimation of smooth vertex trajectories: In this section, we present a methodology to track the set of mesh vertices during the bladder deformations. This is done using the

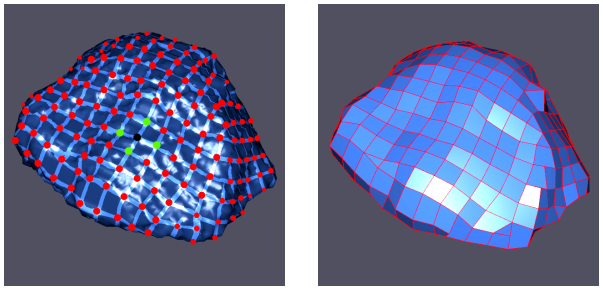

Fig. 1. Quadrilateral mesh for the organ, from left to right: the position field, and the output mesh.

LDDMM framework that has been heuristically shown to produce natural deformation paths compatible with the physics of deformations. A smooth and continuous-time trajectory of each vertex is estimated throughout the organ range of motion. The LDDMM framework can be used for manipulating dense imagery and for tracking a dynamic set of feature points over a long dynamic MRI sequence. The bladder deformation can be interpreted and parameterized using a control-points-based LDDMM method for constructing diffeomorphisms of the ambient space $\mathbb{R}^3$. This framework estimates a smooth and invertible deformation field which maps a shape to another one without having to use point-to-point correspondence.

The principle of control-points-based LDDMM for estimating a diffeomorphic mapping is as follows:
Given a set of N control points $\{q_i\}_{i\in 1,\dots,N}$, and a set of N corresponding momentum vectors of $\mathbb{R}^3$ $\{\mu_i\}_{i\in 1,\dots,N}$, the velocity vector in the tangent space $\mathcal{T}_x\mathcal{M}$ of the parametric surface $\mathcal{M}$ at a point $x \in \mathcal{M}$, is obtained through the use of a Gaussian convolution filter:

$$v : x \in \mathbb{R}^3 \mapsto v(x) = \sum_{i=1}^{N} K(x, q_i).\mu_i \tag{2}$$

where $K(x_i, x_j) = exp(-||x_i - x_j||^2/\sigma^2)$ is a gaussian kernel.

The temporal evolution of the organ velocity vector field can be modeled by the following Hamilton's equations of motion:

$$\begin{cases} \dot{q}(t) = K(q(t), q(t)).\mu(t) \\ \dot{\mu}(t) = -\frac{1}{2}\nabla_q\{K(q(t), q(t)), \mu(t)^\top \mu(t)\} \end{cases} \tag{3}$$

Solving this pair of PDEs using a second-order Runge-Kutta scheme gives a smooth temporal velocity vector field parameterized with $q(t)$ and $\mu(t)$:

$$v : x \in \mathbb{R}^3 \times t \in [0, 1] \mapsto v(x, t) = \sum_{i=1}^{N} K(x, q_i(t)).\mu_i(t) \tag{4}$$

The temporal displacement of each tracked point $x \in \mathcal{M}$ is governed by the following ODE:

$$\dot{x}(t) = v(x(t), t) \tag{5}$$

with the initial condition $x(0) = x$.

Finally, the solution of this ODE yields a flow of diffeomorphisms starting from the source points (i.e. starting from the identity in the space of transformations), $\Phi_{q,\mu}(., t) : \mathbb{R}^3 \times [0, 1] \mapsto \mathbb{R}^3$, such that $\Phi_{q,\mu}(., 1) = Id + \int_0^1 v(\Phi_{q,\mu}(., t))dt$ is the end-point of the geodesic flow matching the given point sets.

The overall algorithm for point tracking is described in Algorithm 1, with the following notations: L is the length of the dynamic sequence; $\mathcal{M}_t$ gives the locations of the point set being tracked at time t; $\mathcal{C}_t$ is the entire 3D surface point cloud at time t; where $\mathcal{M}_t$ is a proper subset of $\mathcal{C}_t$. Note that the registration problem is solved by iteratively minimizing the following loss function:

$$f(q, \mu) = d(\mathcal{C}_{t+1}, \Phi_{q,\mu}(\mathcal{M}_t)) + R(q, \mu) \tag{6}$$

where the first term measures data-attachment while the second regularization term represents the norm of the deformation. An illustration is given in Fig. 2.

Algorithm 1 Tracking of mesh vertices

Input: Mesh vertices $\mathcal{M}_0$.
Motion estimation: Estimate forward successive point trajectories using the LDDMM $\{\mathcal{M}_{t+1}\}_{t=0,\dots,L-1}$ such that $\mathcal{M}_t \subset \mathcal{C}_t$, for $t = 0, \dots, L-1$, by aligning $\mathcal{M}_t$ and $\mathcal{C}_{t+1}$.

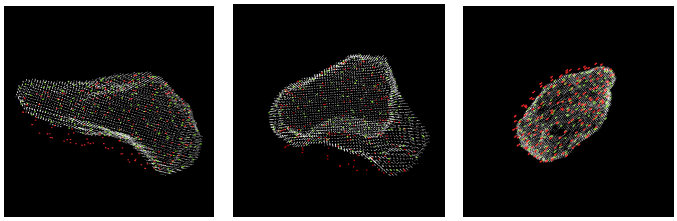

Fig. 2. Pointset tracking: : $\mathcal{M}_0$ in red, $\mathcal{M}_t$ in green, and $\mathcal{C}_t$ in white.

B. Feature analysis: a novel geometric feature type

In this section, we propose a robust global feature to detect the surface variation in terms of concavity and convexity with smooth transitions in-betweens by minimizing the Dirichlet energy inside the surface between shape and a surrounding sphere. This gives a set of paths of minimum Dirichlet energy (*i.e.* a set of geodesics) that are used to map a shape to a sphere.

Definition Let Ω be a bounded, smooth open subset of $\mathbb{R}^n$. And let $h : \Omega \to \mathbb{R}$ be a differentiable function over Ω, the Dirichlet energy of h is defined by the following quantity:

$$E[h] = \frac{1}{2}\int_{x\in\Omega} ||\nabla h(x))||^2 dx \tag{7}$$

where $\nabla h : \Omega \to \mathbb{R}^n$ is the gradient vector field of h.
Solving Laplace's equation $\Delta h(x) = 0$, $\forall x \in \Omega$, subject to appropriate Dirichlet boundary conditions, is equivalent to solving the variational problem of finding a function h that satisfies the boundary conditions and has minimal Dirichlet energy.
For a closed 3D shape S, the *proposed* feature can be numerically approximated using an Eulerian PDE approach, involving the following steps.

Definition of Dirichlet boundary conditions:

To initialize the algorithm, the binary mask of the shape is eroded with a cross-shaped structuring element which is best suited for fine structures. The choice of the structuring element is of great importance for preserving, as much as possible, the topology of any arbitrary shape. This gives the eroded binary mask that we note S_e. Then, we use a PCA analysis of S in order to determine the radius R of the surrounding sphere S_s centered at the shape centroid. The radius R is proportional to the length of the principal axis of inertia l ($R = 0.8l$). At this level, all the surface points will be located between two non-intersecting boundaries: $S_{in} = S_e$, and $S_{out} = \bar{S}_s$.
The next step consists of computing the length of the shortest geodesic paths from S_{in} to S_{out} in a bijective fashion.

Solving the Laplace equation, subject to Dirichlet boundary conditions:

This primordial step consists of solving the Dirichlet problem, also known as the problem of finding a function which solves a specified PDE inside a region that takes prescribed values on its boundaries. The Dirichlet energy is intimately connected to Laplace's equation. In practice, we are looking for an elliptic twice-differentiable function $h : \mathbb{R}^3 \rightarrow \mathbb{R}$ which satisfies the Laplace's PDE $\Delta h = div(grad(h)) = 0$ inside the region $\Omega = \overline{S_{in} \cup S_{out}}$, subject to the Dirichlet boundary conditions $h(\partial S_{in}) = 10^4$ and $h(\partial S_{out}) = 0$. The physical intuition behind is to determine the equilibrium heat distribution in a perfectly symmetric spherical room since the divergence of the gradient vector field corresponds to some kind of fluid flow.
To approximate the numerical solution of Laplace's equation, we use the Jacobi iterative relaxation method which is simple to implement and which allows fast approximation of the solution in cartesian coordinates:

$$h_{t+1}(i,j,k) = \frac{1}{2(d_i^2 d_j^2 + d_i^2 d_k^2 + d_j^2 d_k^2)} (d_j^2 d_k^2 [h_t(i + d_i, j, k) + h_t(i - d_i, j, k)] + d_i^2 d_k^2 [h_t(i, j + d_j, k) + h_t(i, j - d_j, k)] + d_i^2 d_j^2 [h_t(i, j, k + d_k) + h_t(i, j, k - d_k)]) \quad (8)$$

where t is the iteration index. In this work, we process reconstructed data with an isotropic voxel spacing of $1 \times 1 \times 1mm$ (*i.e.* $d_i = d_j = d_k = 1$).

Computing the normal vectors to the tangent planes to the harmonic layers:

Determine elementary normal paths from S_{in} to S_{out}, *i.e.* from the normalized gradient vector field of the harmonic interpolant h, $\vec{T} = \frac{\nabla h}{\|\nabla h\|} = (T_i, T_j, T_k)^T$. This velocity vector field corresponds to a one-to-one mapping.

An Eulerian PDE computational scheme:

We estimate the lengths of optimal geodesic paths between the two boundaries, by solving a couple of PDEs: $\nabla L_0 . \vec{T} = -\nabla L_1 . \vec{T} = 1$. L_0 and L_1 are first initialized to 0.5 and then iteratively updated using a symmetric relaxation Gauss-Seidel method:

$$\frac{L_0^{t+1}[i,j,k]}{\alpha} = 1 + |T_i| L_0^t[i \mp 1, j, k] + |T_j| L_0^t[i, j \mp 1, k] + |T_k| L_0^t[i, j, k \mp 1] \quad (9)$$

$$\frac{L_1^{t+1}[i,j,k]}{\alpha} = 1 + |T_i| L_1^t[i \pm 1, j, k] + |T_j| L_1^t[i, j \pm 1, k] + |T_k| L_1^t[i, j, k \pm 1] \quad (10)$$

where: $\begin{cases} m \pm 1 = m + sgn(T_m); m \mp 1 = m - sgn(T_m) \\ for \quad m \in \{i,j,k\}; \quad and \quad \alpha = \frac{1}{|T_i| + |T_j| + |T_k|} \end{cases}$

with: $sgn(.)$ is the sign function, $L_0(x)$ is the length of the optimal geodesic path from the point $x = (i,j,k)$ to S_{in}, while $L_1(x)$ is the length of the optimal geodesic path from x to S_{out}. The sum of these two lengths $G(x) = L_0(x) + L_1(x)$, defined as *thickness* in [10], represents in fact the length of the optimal geodesic path from S_{in} to S_{out} that passes through x. These geometric methods which are based on a fully Eulerian point of view allow one to handle time derivatives with finite differences in a bounded physical domain that exhibit large deformations and topology changes.

Convergence criterion:

The numerical solution of Laplace's equation is iteratively relaxed by finite differences. All grid points inside Ω are visited at each iteration. A convergence criterion can be defined by the following expression based on the total field energy over Ω: $\epsilon_t = \sum_{x \in \Omega} \sqrt{(\frac{\Delta h_t}{di})^2 + (\frac{\Delta h_t}{dj})^2 + (\frac{\Delta h_t}{dk})^2}$, where $\frac{\Delta h_t}{di} = \frac{h_t(i+di,j,k) - h_t(i-di,j,k)}{2}$. The Jacobi iterative computational scheme of eq (8) converges when the ratio $\epsilon = \frac{\epsilon_t - \epsilon_{t+1}}{\epsilon_t}$ becomes smaller than a user-defined threshold (typically about 10^{-5}). To speed up the algorithm, we strongly recommend to keep the number of iterations as a user defined parameter in order to avoid the repeated evaluation of ϵ at each iteration. A total number of 200 iterations is used for solving the Laplace's equation and the pair of PDEs in this work.

Proposed feature to characterizing the surface variation:

Finally, we define a flexible feature by the following application $\tilde{f} : \mathbb{R}^3 \rightarrow \mathbb{R}$:

$$\tilde{f}(x) = \frac{R}{G(x)} \quad (11)$$

Note that $L_1 >> L_0$ for all the surface points so that $G \simeq L_1$ and only one PDE has to be solved to calculate the feature function. The function $\tilde{f}$ has the potential to characterize the surface variation and to delineate between concave, convex and flat regions with smooth transitions in-between, as illustrated in Fig 6 for both torus and ellipsoid. Relatively, the largest feature values correspond to the most convex areas in the surface while the smallest values correspond to the most concave areas. Furthermore, this feature is invariant to scale since the sphere radius is proportional to the length of the principal axis of inertia of the shape; invariant to rotation thanks to spherical symmetry; and also invariant to translation since the sphere center coincides with the shape centroid. An illustration of all the previous steps is presented in Fig. 3.

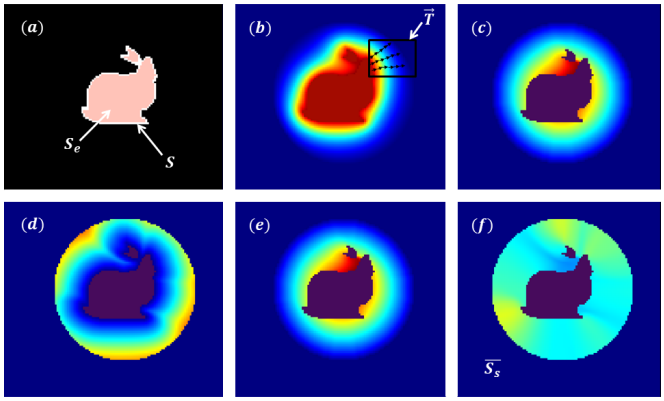

Fig. 3. Proposed method (Stanford Bunny example): (a) binary mask and its eroded; (b) solution of the Laplace equation h; (c) length of the geodesic path from x to the surrounding sphere L_1; (d) length of the geodesic path from x to the inner boundary L_0; (e) length of the resulting geodesic path G; and (f) feature values $\tilde{f}$ between the two boundaries.

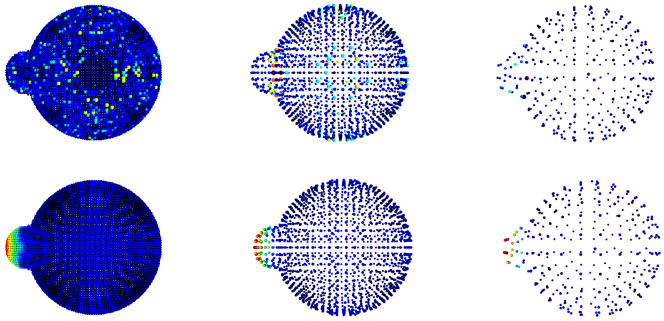

Fig. 4. Local characterization of 3D surfaces. First row: the covariance-based shape curvature with 4-nearest neighbors. Second row: our proposed feature based on the geodesic distances. The columns show the robustness of our metric face to the point cloud density: first column: voxel size equal to 1 (*i.e.*, we keep all the contour points), second column: with a voxel size of 3, and with a voxel size of 7 in the third column.

IV. Experiments and Results

A. Data set

Pelvis areas of six healthy participants were imaged with a 1.5T MRI scanner (MAGNETOM Avanto, Siemens AG, Healthcare Sector, Erlangen, Germany) using a spine/phased array coil combination. T_1/T_2W bSSFP images (TR: 125 ms, echo time: 1.25 ms, flip angle: 52°, field of view: 299 x 350 mm^2, pixel size: 1.36 x 1.36 mm^2, slice thickness: 6 mm, multi-planar configuration) were recorded during a 1:20-minutes forced breathing exercise. During this exercise, the subject alternately inspired and expired at maximum capacity. Subjects were also instructed to increase the pelvic pressure to the maximum inspiration and contrary to contract the pelvic floor during the expiration. These actions increased the intra-abdominal pressure, causing deformities of the pelvic organs. The study was approved by the local human research committee and was conducted in conformity with the Declaration of Helsinki. Since no extrageneous liquids was injected into pelvic cavities in this study, only the segmentation of the bladder was performed and the analysis focused exclusively on this organ. For each subject, the three-dimensional dynamic sequences acquired in multi-planar configurations allowed the reconstruction of nearly 400 bladder volumes generated at a rate of 8 volumes per second.

B. Validating the point-tracking process

The parameters of our registration algorithm are set as follows: the standard deviation of the Gaussian kernel defined in (2) is set to $\sigma = 10^{-4}$ in order to obtain a deformation field with a very thin level of precision. The kernel-width parameter for controlling the granularity of the deformation is set to 8. 15 intermediate states describing the temporal evolution of the tracked points are estimated in order to obtain a smooth continuous-time trajectory of the organ shape between successive time frames. The loss function defined in (6) is minimized using the gradient ascent optimization method. All experiments are performed on an Intel® Xeon® Processor Silver 4214 CPU @ 2.20GHz, with a physical memory of 93GB. For the first subject for example, Algorithm 1 takes 6 sec to align a set of 342 tracked point set $\mathcal{M}_t$, with the target set $\mathcal{C}_t$, composed of 5686 points for which only a set of 210 control points have been used for optimizing the shape matching.

To validate the tracking process, we propose to compute the following error:

$$E = \frac{1}{N}\sum_{p=1}^{N} dist(x_p, \mathcal{C}_L) \tag{12}$$

where: N is the total number of tracked points; $x_p \in \mathcal{M}_L$; and $dist(x_p, \mathcal{C}_L)$ is the Euclidian ℓ^2 distance between x_p and the closest point x_l in the last reconstructed surface $\mathcal{C}_L$. A propagated mean error of 0.63 ± 0.06 is obtained across all subjects. The resulting error is always inferior to $1mm$ which reflects the tracking accuracy level for a given isotropic voxel size of $1 \times 1 \times 1mm$. Fig. 5 shows the quality of our 3D+t quadrilateral mesh reconstruction based on smoothly tracking vertices using the LDDMM while keeping the mesh faces unchanged.

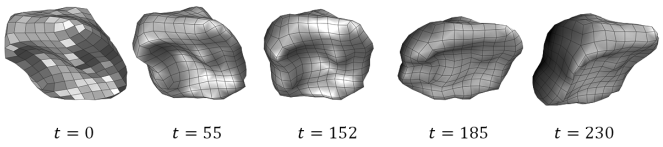

Fig. 5. 4D reconstructed quad mesh during forced respiratory motion.

C. Feature application to synthetic data

The performances of our 3D geometric descriptor are evaluated on some known synthetic surfaces, (see Fig. 6). Since all the covariance-based features, detailed in section II, describe the local surface variation, we compared our 3D geometric descriptor with the surface curvature. The covariance-based curvature is computed using 4-nearest neighbors. Each point neighborhood is determined using a ball tree algorithm. An

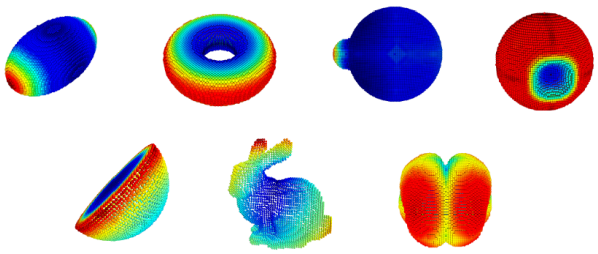

Fig. 6. Feature application to symmetric and non-symmetric 3D shapes.

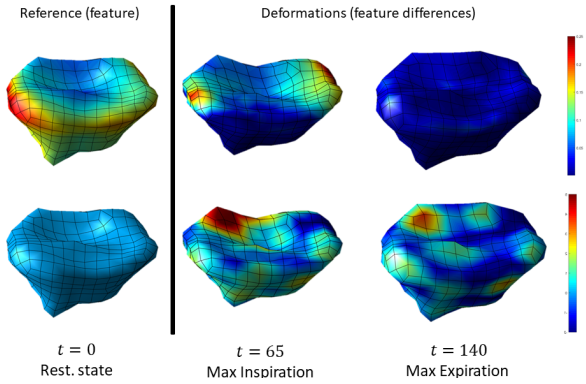

Fig. 7. Characterization of the organ shape variability at mid and extreme range of motion: The first row shows the texture mapping of our geometric feature on bladder meshes, while the second row shows the mesh elongations.

example of a point neighborhood is illustrated in Fig 1 (the black point and its 4-nearest neighbors in green). Fig. 4 shows that contrary to our feature, the covariance-based features become more sensitive to noise with an increase of the total number of surface points.

D. Characterization of bladder deformations

The main application of this study consists of characterizing the bladder deformations during repeated respiratory motion cycles. Fig. 7 illustrates the characterization of the organ shape variability at mid and extreme range of motion: resting state $t = 0$, maximum of inspiration $t = 65$ causing a huge organ contraction, and maximum of expiration $t = 140$ inducing an important bladder swelling. The mapping of our feature as a texture on the reconstructed quadrilateral mesh surface is presented in first row, first column of the figure. Second and third columns show surface motion patterns relative to the reference resting state, highlighting the regions the most affected by deformations. The second row shows the mapping of mesh elongations on the surface w.r.t. the resting state. The elongation also called the Green-Lagrange deformation is a commonly used feature for characterizing local deformations and it measures the level of the spacing in the neighborhood of a point.

In order to characterize the bladder deformations during loading exercises for each subject, we compute our invariant geometric descriptor for the temporal organ surfaces, then we compare each feature map at a time frame t with that of the initial one ($t = 0$) using the Pearson correlation metric. Results presented in Fig. 8 illustrate the temporal correlation curves for three subjects. For each motion cycle, a decrease of the correlation value indicates an organ deformation w.r.t the reference (initial shape), this can be interpreted by the fact that forced inspiration involves an action of the diaphragm and abdominal muscles that induces deformations of the internal pelvic organs. Otherwise, when the correlation values increase, the patient releases the pressure and consequently the bladder relaxes and its surface returns to its initial state ($t = 0$). Taking for example the case of the second subject, for time frames $t \in [0, 30]$, we note a correlation drop down from 1 to 0.9 characterized by an inspiration mode. Beyond t =30 to 50, the increase of correlation values reflects the fact that the subject is in expiration mode. So on, the correlations between the shapes of the bladder vary according to the breathing mode applied by the patient. The presence of noise (especially for S1 and S3) is simply caused by errors of 3D reconstruction of the sequences from dynamic MRI and also due to the instability of the respiratory motion cycles for each subject. Fig. 9 illustrates the temporal evolution of feature values for two surface regions (from S1): a first point p_0 is selected from a non-highly deformable surface region (the bladder neck supported by the pelvic floor muscle). The average feature values in the 8-neighborhood of p_0 are then calculated to evaluate the local behavior of the surface variation around that point. A second point p_1 is selected from a highly deformable lateral region (the apex) so that the corresponding temporal feature curve fluctuated over time. This confirms that our geometric descriptor is capable of separating between surface regions undergoing different deformation rates with respect to the neutral position (resting state).

V. Conclusion

In this paper, we have developed a framework for characterizing the temporal evolution of 3D shapes and we have showed an example of application with data acquired from *in vivo* observations of moving bladder using dynamic MRI sequences. A 4D smooth quad mesh is first established using non-linear diffeomorphic registration. Second, a new geometric feature is proposed to deal with large deformations based on mapping a shape to a sphere. Results demonstrate the robustness of our descriptor no matter how sparse the point cloud may be. Future works will include the calculation of different biomechanical parameters from the obtained dynamical quadrilateral meshes such as distortions, strains and stresses.Furthermore, the pipeline will be applied to characterize other vital organs such as the heart during cardiac motion.

References

[1] M. Rahim, M.-E. Bellemare, R. Bulot, and N. Pirró, "A diffeomorphic mapping based characterization of temporal sequences: application to the pelvic organ dynamics assessment," *Journal of mathematical imaging and vision*, vol. 47, no. 1-2, pp. 151–164, 2013.

[2] K. Makki, B. Borotikar, M. Garetier, S. Brochard, D. B. Salem, and F. Rousseau, "High-resolution temporal reconstruction of ankle joint from dynamic MRI," in *2018 IEEE 15th International Symposium on Biomedical Imaging (ISBI 2018)*, pp. 1297–1300, IEEE, 2018.

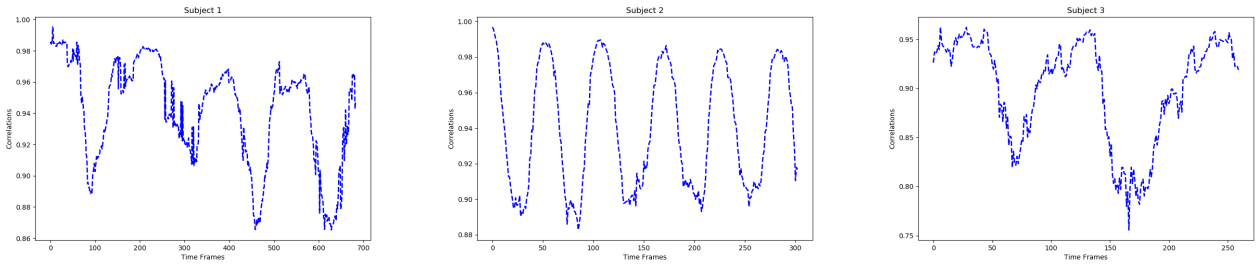

Fig. 8. Correlations between each temporal feature map and the initial one for three subjects.

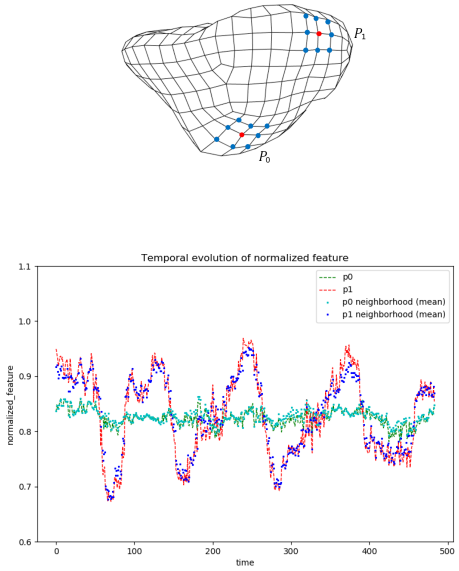

Fig. 9. Normalized feature evolution around two significant points.

[3] K. Makki, B. Borotikar, M. Garetier, S. Brochard, D. B. Salem, and F. Rousseau, "In vivo ankle joint kinematics from dynamic magnetic resonance imaging using a registration-based framework," *Journal of biomechanics*, vol. 86, pp. 193–203, 2019.

[4] A. C. Ogier, S. Rapacchi, A. Le Troter, and M.-E. Bellemare, "3D dynamic MRI for pelvis observation-a first step," in *2019 IEEE 16th International Symposium on Biomedical Imaging (ISBI 2019)*, pp. 1801–1804, IEEE, 2019.

[5] Z. Jiang, O. Mayeur, J.-F. Witz, P. Lecomte-Grosbras, J. Dequidt, M. Cosson, C. Duriez, and M. Brieu, "Virtual image correlation of magnetic resonance images for 3D geometric modelling of pelvic organs," *Strain*, vol. 55, no. 3, p. e12305, 2019.

[6] M. Pauly, M. Gross, and L. P. Kobbelt, "Efficient simplification of point-sampled surfaces," in *IEEE Visualization, 2002. VIS 2002.*, pp. 163–170, IEEE, 2002.

[7] R. Dubé, D. Dugas, E. Stumm, J. Nieto, R. Siegwart, and C. Cadena, "Segmatch: Segment based loop-closure for 3D point clouds," *arXiv preprint arXiv:1609.07720*, 2016.

[8] I. Jovančević, H.-H. Pham, J.-J. Orteu, R. Gilblas, J. Harvent, X. Maurice, and L. Brèthes, "3D point cloud analysis for detection and characterization of defects on airplane exterior surface," *Journal of Nondestructive Evaluation*, vol. 36, no. 4, p. 74, 2017.

[9] Z. Liu, S. Zhou, C. Suo, P. Yin, W. Chen, H. Wang, H. Li, and Y.-H. Liu, "LPD-Net: 3D point cloud learning for large-scale place recognition and environment analysis," in *Proceedings of the IEEE International Conference on Computer Vision*, pp. 2831–2840, 2019.

[10] A. J. Yezzi and J. L. Prince, "An Eulerian PDE approach for computing tissue thickness," *IEEE transactions on medical imaging*, vol. 22, no. 10, pp. 1332–1339, 2003.

[11] F. Pomerleau, F. Colas, R. Siegwart, *et al.*, "A review of point cloud registration algorithms for mobile robotics," *Foundations and Trends® in Robotics*, vol. 4, no. 1, pp. 1–104, 2015.

[12] Y. He, B. Liang, J. He, and S. Li, "Non-cooperative spacecraft pose tracking based on point cloud feature," *Acta Astronautica*, vol. 139, pp. 213–221, 2017.

[13] P. J. Besl and N. D. McKay, "Method for registration of 3D shapes," in *Sensor fusion IV: control paradigms and data structures*, vol. 1611, pp. 586–606, International Society for Optics and Photonics, 1992.

[14] B. Combès and S. Prima, "An efficient EM-ICP algorithm for non-linear registration of large 3D point sets," *Computer Vision and Image Understanding*, vol. 191, p. 102854, 2020.

[15] A. Bône, O. Colliot, and S. Durrleman, "Learning distributions of shape trajectories from longitudinal datasets: a hierarchical model on a manifold of diffeomorphisms," in *Proceedings of the IEEE Conference on Computer Vision and Pattern Recognition*, pp. 9271–9280, 2018.

[16] M. F. Beg, M. I. Miller, A. Trouvé, and L. Younes, "Computing large deformation metric mappings via geodesic flows of diffeomorphisms," *International journal of computer vision*, vol. 61, no. 2, pp. 139–157, 2005.

[17] P. Gori, O. Colliot, L. Marrakchi-Kacem, Y. Worbe, C. Poupon, A. Hartmann, N. Ayache, and S. Durrleman, "A Bayesian framework for joint morphometry of surface and curve meshes in multi-object complexes," *Medical image analysis*, vol. 35, pp. 458–474, 2017.

[18] J. Fishbaugh, S. Durrleman, M. Prastawa, and G. Gerig, "Geodesic shape regression with multiple geometries and sparse parameters," *Medical image analysis*, vol. 39, pp. 1–17, 2017.

[19] J. Mao, X. Wang, and H. Li, "Interpolated convolutional networks for 3D point cloud understanding," in *Proceedings of the IEEE International Conference on Computer Vision*, pp. 1578–1587, 2019.

[20] A. Nurunnabi, G. West, and D. Belton, "Outlier detection and robust normal-curvature estimation in mobile laser scanning 3D point cloud data," *Pattern Recognition*, vol. 48, no. 4, pp. 1404–1419, 2015.

[21] M. Weinmann, B. Jutzi, and C. Mallet, "Geometric features and their relevance for 3D point cloud classification," *ISPRS Annals of the Photogrammetry, Remote Sensing and Spatial Information Sciences*, vol. 4, p. 157, 2017.

[22] H. Zhao, L. Jiang, C.-W. Fu, and J. Jia, "Pointweb: Enhancing local neighborhood features for point cloud processing," in *Proceedings of the IEEE Conference on Computer Vision and Pattern Recognition*, pp. 5565–5573, 2019.

[23] G. Peyré, M. Péchaud, R. Keriven, L. D. Cohen, *et al.*, "Geodesic methods in computer vision and graphics," *Foundations and Trends® in Computer Graphics and Vision*, vol. 5, no. 3–4, pp. 197–397, 2010.

[24] E. Nava-Yazdani, H.-C. Hege, and C. von Tycowicz, "A geodesic mixed effects model in Kendall's shape space," in *Multimodal Brain Image Analysis and Mathematical Foundations of Computational Anatomy*, pp. 209–218, Springer, 2019.

[25] T. Lewiner, H. Lopes, A. W. Vieira, and G. Tavares, "Efficient implementation of marching cubes' cases with topological guarantees," *Journal of graphics tools*, vol. 8, no. 2, pp. 1–15, 2003.

[26] W. Jakob, M. Tarini, D. Panozzo, and O. Sorkine-Hornung, "Instant field-aligned meshes.," *ACM Trans. Graph.*, vol. 34, no. 6, pp. 189–1, 2015.

[27] Z.-W. Chen, P. Joli, Z.-Q. Feng, M. Rahim, N. Pirró, and M.-E. Bellemare, "Female patient-specific finite element modeling of pelvic organ prolapse (POP)," *Journal of biomechanics*, vol. 48, no. 2, pp. 238–245, 2015.